AERODYNAMIC MODEL-FREE WIND ESTIMATION USING A SMALL, FIXED-WING UNCREWED AERIAL VEHICLE

Zakia Ahmed
Graduate Student, Mechanical Engineering
Virginia Tech, Blacksburg, VA, 24061

Craig A. Woolsey
Professor, Aerospace and Ocean Engineering
Virginia Tech, Blacksburg, VA, 24061

Abstract

This paper is concerned with the design of an invariant extended Kalman filter (IEKF) for aerodynamic model-free wind estimation using a small, fixed-wing uncrewed aerial vehicle (UAV). The dynamics and output of the UAV are shown to be left-invariant and left-equivariant, respectively, with respect to transformations on the Lie group $SE(3)$, the space of 3D translations and rotations. The steps for designing the IEKF for the 6DOF rigid aircraft are described and the IEKF is implemented on simulated flight data to obtain wind velocity estimates. The aircraft is simulated subject to a wind field defined by von Kármán turbulence. Wind velocity estimates are obtained using both the IEKF and a conventional extended Kalman filter (EKF) for the aircraft simulated in a non-accelerated helical turn, where it is shown that the IEKF provides more accurate estimates of the wind velocity.

1 Introduction

Measurements of the kinematic and thermodynamic state of the atmospheric boundary layer (ABL) can aid in understanding the natural flow over complex terrain[11], improving numerical weather prediction[14], and support low-altitude aviation missions including urban and advanced air mobility operations. Ground-based weather stations and weather balloons equipped with radiosondes are traditional methods of obtaining atmospheric measurements. Still, they do not provide the flexibility and maneuverability of small uncrewed aerial vehicles (UAVs). Small UAVs are emerging as a promising alternative to conventional atmospheric sensing methods as they offer increased spatial and temporal sampling ability[3,14,18,22,24] as low-cost, *in-situ* ABL sensing platforms. Estimates of the kinematic state of the ABL, specifically the velocity of the mean wind over a region, have been obtained using fixed-wing[9,12,16,23] and multi-rotor[7,13,17,19] aircraft. Radio-controlled (RC) helicopters and multirotor UAVs have also been used to infer the airflow in the wake of ocean vessels[15,21,25].

A small UAV can measure wind velocity directly by mounting dedicated wind sensors such as sonic anemometers on the aircraft. Indirect wind velocity measurements are obtained by considering the aircraft motion in response to wind. Direct measurement can provide accurate wind estimates but it adds weight and cost and the obtained measurements are sensitive to the placement of the sensor and base vehicle motion[26]. Indirect wind velocity measurements use the standard onboard sensor suite including a global navigation satellite system (GNSS) receiver, inertial measurement unit (IMU), magnetometer, and pitot tube, along with a vehicle motion model to estimate the velocity of the wind. Indirect measurements are further classified as model-based[7,10,13,16,20] where a dynamic model is used in the estimation scheme, and model-free[2,8] where no knowledge of the aerodynamic model is required.

Indirect wind estimation methods use filters including the Kalman filter (KF), extended Kalman filter (EKF), and unscented Kalman filter (UKF). This work focuses on indirect model-free wind estimation using an invariant extended Kalman filter (IEKF), based on work by Bonnabel *et al.* on symmetry-preserving observers[5] and later used for attitude estimation of flying rigid bodies[4,6]. The IEKF leverages the symmetries of the dynamic system and uses an adapted invariant output error and invariant state error as opposed to the linear output and state error used in a conventional EKF. This results in constant state and output matrices on a larger subset of the state space when compared to the EKF, which in general, provides stronger convergence guarantees of the IEKF for a larger family of trajectories.

In this paper, a six degree of freedom (6DOF) fixed-wing aircraft model is considered where the UAV motion is perturbed from its nominal condition by some wind field. This work is an extension of a previous work where the IEKF was designed for a 3DOF fixed-wing UAV in constant altitude horizontal-plane flight[1]. Here, the full 6DOF kinematics and dynamics of the UAV are considered and the measurements include GNSS position, attitude, body velocity, and body angular rates. They are described in Section 2. In Section 3 it is proven that the dynamics are invariant, the output is equivariant, and in Section 4, the IEKF is designed for wind estimation. The aircraft is simulated in a von Kármń wind field and a comparison of wind estimation results using an IEKF and an EKF are described in Section 5. Conclusions are made in Section 6.

2 Aircraft Motion and Measurement Models

A 6DOF aircraft in wind is considered in this paper where the goal is to estimate the wind velocity affecting the aircraft's motion. A description of aircraft kinematics and dynamics requires defining the relevant reference frames. We consider the two-dimensional *inertial* and *body-fixed* frames:

- The *inertial* reference frame is given by the orthonormal triad $(\boldsymbol{i}_X, \boldsymbol{i}_Y, \boldsymbol{i}_Z)$. The origin of the inertial frame is fixed and its orientation has been chosen such that the positive $\boldsymbol{i}_X$ axis points towards geographic North, the positive $\boldsymbol{i}_Y$ axis points East, and the positive $\boldsymbol{i}_Z$ axis points down completing the orthonormal frame. The location of the origin of the inertial reference frame is arbitrary.
- The *body-fixed* reference frame is given by the orthonormal triad $(\boldsymbol{b}_x, \boldsymbol{b}_y, \boldsymbol{b}_z)$. The origin of the body-fixed reference frame is the aircraft's center of gravity. The positive $\boldsymbol{b}_x$ axis points forward through the nose of the aircraft. The positive $\boldsymbol{b}_y$ axis points to the right, as viewed from above. The positive $\boldsymbol{b}_z$ axis points down through the underside of the aircraft.

The attitude kinematics and dynamics of a UAV flying in wind are

$$\begin{aligned}
\dot{\boldsymbol{X}} &= \boldsymbol{R}_{\mathrm{IB}}\boldsymbol{v}_{\mathrm{r}} + \boldsymbol{V}_w && \text{(1a)}\\
\dot{\boldsymbol{R}}_{\mathrm{IB}} &= \boldsymbol{R}_{\mathrm{IB}}\boldsymbol{\omega}^{\times} && \text{(1b)}\\
\dot{\boldsymbol{v}}_r &= \boldsymbol{v}_{\mathrm{r}} \times \boldsymbol{\omega} + \boldsymbol{f}_{\mathrm{A}} + \boldsymbol{R}_{\mathrm{IB}}^{\mathrm{T}}\boldsymbol{g} && \text{(1c)}\\
\dot{\boldsymbol{\omega}} &= \boldsymbol{I}^{-1}\left(\boldsymbol{I}\boldsymbol{\omega} \times \boldsymbol{\omega}\right) + \boldsymbol{m}_{\mathrm{A}} && \text{(1d)}\\
\dot{\boldsymbol{V}}_w &= \boldsymbol{0} && \text{(1e)}
\end{aligned}$$

where $\boldsymbol{X} = (X, Y, Z)^{\mathrm{T}} \in \mathbb{R}^3$ denotes the inertial position of the UAV, $\boldsymbol{v}_{\mathrm{r}} = (v_{r,x}, v_{r,y}, v_{r,z})^{\mathrm{T}} \in \mathbb{R}^3$ is the air-relative velocity vector expressed in the body-fixed reference frame, $\boldsymbol{\omega} = (p, q, r)^{\mathrm{T}} \in \mathbb{R}^3$ is the angular velocity expressed in the body frame, and $\boldsymbol{V}_w = (V_{w,x}, V_{w,y}, V_{w,z})^{\mathrm{T}} \in \mathbb{R}^3$ is the wind velocity expressed in the inertial frame. The rotation matrix $\boldsymbol{R}_{\mathrm{IB}} \in SO(3)$ maps free vectors expressed in the body-fixed frame to the inertial frame. The matrix $\boldsymbol{R}_{BI}$ that maps vectors from the inertial frame to the body-fixed frame is $\boldsymbol{R}_{BI} = \boldsymbol{R}_{\mathrm{IB}}^{-1} = \boldsymbol{R}_{\mathrm{IB}}^{\mathrm{T}}$. The notation $(\cdot)^{\times}$ denotes the *cross-product equivalent matrix* satisfying $\boldsymbol{a}^{\times}\boldsymbol{b} = \boldsymbol{a} \times \boldsymbol{b}$ for 3×1 vectors $\boldsymbol{a}$ and $\boldsymbol{b}$. For the vector $\boldsymbol{\omega}$, for example, we have

$$\boldsymbol{\omega}^{\times} = \begin{pmatrix} 0 & -r & q \\ r & 0 & -p \\ -q & p & 0 \end{pmatrix}$$

The term $\boldsymbol{f}_{\mathrm{A}}$ in (1c) represents the *specific force* – force divided by mass – acting on the aircraft due to aerodynamic effects such as thrust, drag, side force, and lift. Similarly, $\boldsymbol{m}_{\mathrm{A}}$ in (1d) represents the *specific moment* – moment premultiplied by inverse inertia – due to aerodynamic effects such as pitch stiffness and yaw damping. The vector $\boldsymbol{g} = (0, 0, g)^{\mathrm{T}}$ is the specific force due to gravity, where g is the magnitude of gravitational acceleration.

The system (1) can be written in first-order form as

$$\dot{\boldsymbol{x}} = \boldsymbol{f}(\boldsymbol{x}, \boldsymbol{u}) = \begin{pmatrix} \boldsymbol{R}_{\mathrm{IB}}\boldsymbol{v}_{\mathrm{r}} + \boldsymbol{V}_w \\ \boldsymbol{R}_{\mathrm{IB}}\boldsymbol{\omega}^{\times} \\ \boldsymbol{v}_{\mathrm{r}} \times \boldsymbol{\omega} + \boldsymbol{f}_{\mathrm{A}} + \boldsymbol{R}_{\mathrm{IB}}^{\mathrm{T}}\boldsymbol{g} \\ \boldsymbol{I}^{-1}\left(\boldsymbol{I}\boldsymbol{\omega} \times \boldsymbol{\omega}\right) + \boldsymbol{m}_{\mathrm{A}} \\ \boldsymbol{0} \end{pmatrix} \tag{2}$$

where the state $\boldsymbol{x} \in \mathbb{R}^{n=15}$ and input $\boldsymbol{u} \in \mathbb{R}^{p=6}$ are

$$\boldsymbol{x} = \begin{pmatrix} \boldsymbol{X} \\ \boldsymbol{R}_{\mathrm{IB}} \\ \boldsymbol{v}_{\mathrm{r}} \\ \boldsymbol{\omega} \\ \boldsymbol{V}_w \end{pmatrix} \quad \text{and} \quad \boldsymbol{u} = \begin{pmatrix} \boldsymbol{f}_{\mathrm{A}} \\ \boldsymbol{m}_{\mathrm{A}} \end{pmatrix} \tag{3}$$

We assume that the UAV is equipped with a GNSS receiver, IMU, magnetometer, and 5-hole probe. The measurement equation $\boldsymbol{y} \in \mathbb{R}^{q=18}$ is

$$\boldsymbol{y} = \boldsymbol{h}(\boldsymbol{x}, \boldsymbol{u}) = \begin{pmatrix} \boldsymbol{X} \\ \boldsymbol{R}_{\mathrm{IB}} \\ \boldsymbol{v}_{\mathrm{r}} \\ \boldsymbol{\omega} \end{pmatrix} \tag{4}$$

Note that the problem formulation assumes that $\boldsymbol{f}_{\mathrm{A}}$ and $\boldsymbol{m}_{\mathrm{A}}$ can be directly measured, e.g., using linear and angular accelerometers, so that aerodynamic force and moment models are not required.

3 Proof of Invariant Dynamics and Equivariant Output

The invariance of the dynamics (1) and equivariance of the measurements (4) are established with respect to the Lie group $SE(3)$ in this section. The Lie group $SE(3)$ is the space of 3D translations and rotations, which is the configuration manifold for the fixed-wing UAV where we assume planar motion. Let $g = (\boldsymbol{X}_g, \boldsymbol{R}_g) \in G = SE(3)$ where $\boldsymbol{X}_g \in \mathbb{R}^3$ denotes the position of the aircraft and where $\boldsymbol{R}_g \in SO(3)$ is parameterized by the

Euler angles $(\phi_g, \theta_g, \psi_g)$.

Definition 1. (Adapted from Bonnabel *et al.*[5]). Given a Lie group G, the system

$$\begin{aligned} \dot{\boldsymbol{x}} &= \boldsymbol{f}(\boldsymbol{x}, \boldsymbol{u}) \\ \boldsymbol{y} &= \boldsymbol{h}(\boldsymbol{x}, \boldsymbol{u}) \end{aligned}$$

has *G-invariant dynamics* and *G-equivariant output* if there exist transformations $\boldsymbol{\phi}_g(\boldsymbol{x}(t))$ and $\boldsymbol{\psi}_g(\boldsymbol{u}(t))$ on the state and input, respectively, such that

$$\begin{aligned} D\boldsymbol{\phi}_g(\boldsymbol{x}) \cdot \boldsymbol{f}(\boldsymbol{x}, \boldsymbol{u}) &= \boldsymbol{f}(\boldsymbol{\phi}_g(\boldsymbol{x}), \boldsymbol{\psi}_g(\boldsymbol{u})) \quad \text{(5a)} \\ \boldsymbol{\rho}_g(\boldsymbol{y}) &= \boldsymbol{h}(\boldsymbol{\phi}_g(\boldsymbol{x}), \boldsymbol{\psi}_g(\boldsymbol{u})) \quad \text{(5b)} \end{aligned}$$

for all $g \in G, \boldsymbol{x}$, and $\boldsymbol{u}$. The invariance property also reads $\frac{d}{dt}\boldsymbol{\mathcal{X}} = \boldsymbol{f}(\boldsymbol{\mathcal{X}}, \boldsymbol{\psi}_g(\boldsymbol{u}))$ for $\boldsymbol{\mathcal{X}} = \boldsymbol{\phi}_g(\boldsymbol{x})$.

This work considers the left action of $G = SE(3)$ on the state and input of the aircraft, *i.e.*, the state and input transformations $\boldsymbol{\phi}_g$ and $\boldsymbol{\psi}_g$ represent transformations under the left action of $G = SE(3)$. To fix notation, we let $\boldsymbol{g} = (\boldsymbol{X}_g, \boldsymbol{R}_g) \in G = SE(3)$ where $\boldsymbol{X}_g \in \mathbb{R}^3$ and $\boldsymbol{R}_g \in SO(3)$.

Proposition 1. *The dynamics (2) are invariant under the left action of $SE(3)$ on the state and input as given below:*

$$\boldsymbol{\phi}_g(\boldsymbol{x}) = \begin{pmatrix} \boldsymbol{X}_g + \boldsymbol{X} \\ \boldsymbol{R}_{IB}\boldsymbol{R}_g^{\mathrm{T}} \\ \boldsymbol{R}_g\boldsymbol{v}_{\mathrm{r}} \\ \boldsymbol{R}_g\boldsymbol{\omega} \\ \boldsymbol{V}_w \end{pmatrix} \tag{6}$$

and

$$\boldsymbol{\psi}_g(\boldsymbol{u}) = \begin{pmatrix} \boldsymbol{R}_g\boldsymbol{f}_{\mathrm{A}} \\ \boldsymbol{R}_g\boldsymbol{m}_{\mathrm{A}} \end{pmatrix} \tag{7}$$

Proof. According to (5a) in Definition 1 with state and input transformations (6) and (7), respectively, the system is invariant if it satisfies the condition $\frac{d}{dt}\left(\boldsymbol{\phi}_g(\boldsymbol{x})\right) = \boldsymbol{f}(\boldsymbol{\phi}_g(\boldsymbol{x}), \boldsymbol{\psi}_g(\boldsymbol{u}))$ for all $g \in G$ and for all $\boldsymbol{x}$ and $\boldsymbol{u}$. Differentiating (6) on the left and evaluating $\boldsymbol{f}(\boldsymbol{\phi}_g(\boldsymbol{x}), \boldsymbol{\psi}_g(\boldsymbol{u}))$ on the right where $\boldsymbol{f}$ is given in (2) gives

$$\frac{d}{dt}\begin{pmatrix} \boldsymbol{X} + \boldsymbol{X}_g \\ \boldsymbol{R}_{\mathrm{IB}}\boldsymbol{R}_g^{\mathrm{T}} \\ \boldsymbol{R}_g\boldsymbol{v}_{\mathrm{r}} \\ \boldsymbol{R}_g\boldsymbol{\omega} \\ \boldsymbol{V}_w \end{pmatrix}$$

$$= \begin{pmatrix} \boldsymbol{R}_{\mathrm{IB}}\boldsymbol{R}_g^{\mathrm{T}}\boldsymbol{R}_g\boldsymbol{v}_{\mathrm{r}} + \boldsymbol{V}_w \\ \boldsymbol{R}_{\mathrm{IB}}\boldsymbol{R}_g^{\mathrm{T}}\boldsymbol{R}_g\boldsymbol{\omega}^{\times}\boldsymbol{R}_g^{\mathrm{T}} \\ \boldsymbol{R}_g\boldsymbol{v}_{\mathrm{r}} \times \boldsymbol{R}_g\boldsymbol{\omega} + \boldsymbol{R}_g\boldsymbol{f}_{\mathrm{A}} + \boldsymbol{R}_g\boldsymbol{R}_{\mathrm{IB}}^{\mathrm{T}}\boldsymbol{g} \\ \boldsymbol{R}_g\boldsymbol{I}^{-1}\boldsymbol{R}_g^{\mathrm{T}}\left(\boldsymbol{R}_g\boldsymbol{I}\boldsymbol{R}_g^{\mathrm{T}}\boldsymbol{R}_g\boldsymbol{\omega} \times \boldsymbol{R}_g\boldsymbol{\omega}\right) + \boldsymbol{R}_g\boldsymbol{m}_{\mathrm{A}} \\ \boldsymbol{0} \end{pmatrix}$$

or

$$\begin{pmatrix} \dot{\boldsymbol{X}} \\ \dot{\boldsymbol{R}}_{\mathrm{IB}}\boldsymbol{R}_g^{\mathrm{T}} \\ \boldsymbol{R}_g\dot{\boldsymbol{v}}_r \\ \boldsymbol{R}_g\dot{\boldsymbol{\omega}} \\ \dot{\boldsymbol{V}}_w \end{pmatrix} = \begin{pmatrix} \boldsymbol{R}_{\mathrm{IB}}\boldsymbol{v}_{\mathrm{r}} + \boldsymbol{V}_w \\ \boldsymbol{R}_{\mathrm{IB}}\boldsymbol{\omega}^{\times}\boldsymbol{R}_g^{\mathrm{T}} \\ \boldsymbol{R}_g(\boldsymbol{v}_{\mathrm{r}} \times \boldsymbol{\omega} + \boldsymbol{f}_{\mathrm{A}} + \boldsymbol{R}_{\mathrm{IB}}^{\mathrm{T}}\boldsymbol{g}) \\ \boldsymbol{R}_g(\boldsymbol{I}^{-1}(\boldsymbol{I}\boldsymbol{\omega} \times \boldsymbol{\omega}) + \boldsymbol{m}_{\mathrm{A}}) \\ \boldsymbol{0} \end{pmatrix}$$

The dynamics under the transformations $\boldsymbol{\phi}_g$ and $\boldsymbol{\psi}_g$ satisfy the condition (5a), thus the system described by Eqs. $(1a)-(1e)$ is invariant under the transformations (6) and (7). □

Proposition 2. *The output (4) is equivariant under the left action of $SE(3)$ with state and input transformations $\boldsymbol{\phi}_g(\boldsymbol{x})$ and $\boldsymbol{\psi}_g(\boldsymbol{u})$, respectively, with output transformation*

$$\boldsymbol{\rho}_g(\boldsymbol{y}) = \begin{pmatrix} \boldsymbol{X} + \boldsymbol{X}_g \\ \boldsymbol{R}_{\mathrm{IB}}\boldsymbol{R}_g^{\mathrm{T}} \\ \boldsymbol{R}_g\boldsymbol{v}_{\mathrm{r}} \\ \boldsymbol{R}_g\boldsymbol{\omega} \end{pmatrix} \tag{8}$$

Proof. Using the defined output transformation (8) we show that condition (5b) is satisfied for the output $\boldsymbol{y}$ given in (4).

$$\begin{aligned} \boldsymbol{\rho}_g(\boldsymbol{y}) &= \boldsymbol{y}(\boldsymbol{\phi}_g(\boldsymbol{x}), \boldsymbol{\psi}_g(\boldsymbol{u})) \\ \begin{pmatrix} \boldsymbol{X} + \boldsymbol{X}_g \\ \boldsymbol{R}_{\mathrm{IB}}\boldsymbol{R}_g^{\mathrm{T}} \\ \boldsymbol{R}_g\boldsymbol{v}_{\mathrm{r}} \\ \boldsymbol{R}_g\boldsymbol{\omega} \end{pmatrix} &= \begin{pmatrix} \boldsymbol{X} + \boldsymbol{X}_g \\ \boldsymbol{R}_{\mathrm{IB}}\boldsymbol{R}_g^{\mathrm{T}} \\ \boldsymbol{R}_g\boldsymbol{v}_{\mathrm{r}} \\ \boldsymbol{R}_g\boldsymbol{\omega} \end{pmatrix} \end{aligned}$$

The transformed output satisfies the condition (5b), thus the output equation (4) is $SE(3)$-equivariant. □

It has been shown that a fixed-wing UAV flying in a constant wind field is invariant under the left action of $SE(3)$ and the given measurements are $SE(3)$-equivariant. In the following section, the $SE(3)$-invariant dynamics and $SE(3)$-equivariant output are used to design the invariant EKF.

4 The Invariant Extended Kalman Filter

The IEKF for the fixed-wing UAV is designed using the G-invariant dynamics and G-equivariant measurements from Section 3. In developing the IEKF for a fixed-wing aircraft, we first rewrite the attitude kinematics in the matrix differential equation (1b) in the vector form:

$$\dot{\boldsymbol{\Theta}} = \underbrace{\begin{pmatrix} 1 & \sin\phi\tan\theta & \cos\phi\tan\theta \\ 0 & \cos\phi & -\sin\phi \\ 0 & \sin\phi\sec\theta & \cos\phi\sec\theta \end{pmatrix}}_{\boldsymbol{L}_{\mathrm{IB}}(\boldsymbol{\Theta})}\boldsymbol{\omega} \tag{9}$$

where $\boldsymbol{\Theta} = (\phi, \theta, \psi)^{\mathrm{T}} \in \mathbb{R}^3$ contains the roll, pitch, and yaw angles that parameterize the rotation matrix $\boldsymbol{R}_{\mathrm{IB}}$ as follows:

$$\boldsymbol{R}_{\mathrm{IB}}(\boldsymbol{\Theta}) = \begin{pmatrix} \mathrm{c}\theta\mathrm{c}\psi & \mathrm{c}\psi\mathrm{s}\theta\mathrm{s}\phi - \mathrm{c}\phi\mathrm{s}\psi & \mathrm{c}\psi\mathrm{s}\theta\mathrm{c}\phi + \mathrm{s}\phi\mathrm{s}\psi \\ \mathrm{c}\theta\mathrm{s}\psi & \mathrm{s}\phi\mathrm{s}\theta\mathrm{s}\psi + \mathrm{c}\phi\mathrm{c}\psi & \mathrm{s}\theta\mathrm{c}\phi\mathrm{s}\psi - \mathrm{s}\phi\mathrm{c}\psi \\ -\mathrm{s}\theta & \mathrm{c}\theta\mathrm{s}\phi & \mathrm{c}\theta\mathrm{c}\phi \end{pmatrix} \tag{10}$$

The design of the IEKF is summarized by the following steps[5]:

1. Solve the *normalization equations*.
2. Build an *invariant output error* and a set of *scalar invariants*.
3. Build the *invariant frame*.
4. Define an *invariant state estimate error* and then, using the *pre-observer* defined in Bonnabel *et al.*[5], determine the *invariant state error dynamics*.
5. Design the IEKF by linearizing the invariant state error dynamics and invariant output error about zero state error.

A detailed description of the five steps and application to a fixed-wing UAV in horizontal-plane flight can be found in Ahmed and Woolsey[1]. The dynamic and measurement models have been modified for this paper to include the full 6DOF motion of the UAV. The completion of the above steps using the modified dynamic and measurement equations (1) and (4), respectively, is left as an exercise for the reader. The state matrix for the IEKF is given in (11). where $\mathbf{0}_3$ denotes a 3×3 matrix of zeros. We also obtain the output matrix

$$\boldsymbol{H}_k = \left.\frac{\partial \boldsymbol{E}}{\partial \boldsymbol{\eta}}\right|_{\boldsymbol{\eta}=\mathbf{0}} = \begin{pmatrix} \mathbb{I}_3 & \mathbf{0}_3 & \mathbf{0}_3 & \mathbf{0}_3 & \mathbf{0}_3 \\ \mathbf{0}_3 & \mathbb{I}_3 & \mathbf{0}_3 & \mathbf{0}_3 & \mathbf{0}_3 \\ \mathbf{0}_3 & \mathbf{0}_3 & \mathbb{I}_3 & \mathbf{0}_3 & \mathbf{0}_3 \\ \mathbf{0}_3 & \mathbf{0}_3 & \mathbf{0}_3 & \mathbb{I}_3 & \mathbf{0}_3 \end{pmatrix} \tag{12}$$

The iterative sequence of the IEKF algorithm is provided in Ahmed and Woolsey[1]. The IEKF is obtained by augmenting the symmetry-preserving pre-observer with zero-mean Gaussian white process noise $\tilde{\boldsymbol{w}}$ with covariance matrix $\boldsymbol{Q}$ and augmenting the measurement with zero-mean Gaussian white measurement noise $\tilde{\boldsymbol{v}}$ with covariance matrix $\boldsymbol{R}$.

5 Simulation Results and Discussion

Fixed-wing UAV motion was simulated for a non-accelerated helical turn. The flight dynamic model structure and parameter values are given in Appendix A. In all simulations, the nominal airspeed is $V_{\mathrm{t}} = ||\boldsymbol{v}_{\mathrm{r}}|| = 20$ m/s but a 1D von Kármán wind field is superimposed so that the aircraft is continually perturbed from its nominal state of motion.

The 1D von Kármán turbulence model is characterized by power spectral density functions of spatial frequencies Ω. Assuming that the nominal aircraft motion is due North, the gust spectrum components in the North, East, and down directions are, respectively,

$$\Phi_{11}(\Omega) = \frac{L\sigma^2}{\pi}\frac{1}{(1+(1.339L\Omega)^2)^{5/6}} \tag{13a}$$

$$\Phi_{22}(\Omega) = \frac{L\sigma^2}{2\pi}\frac{1+\frac{8}{3}(1.339L\Omega)^2}{(1+(1.339L\Omega)^2)^{11/6}} \tag{13b}$$

$$\Phi_{33}(\Omega) = \frac{L\sigma^2}{2\pi}\frac{1+\frac{8}{3}(1.339L\Omega)^2}{(1+(1.339L\Omega)^2)^{11/6}} \tag{13c}$$

where L is the turbulence length scale in feet, σ is the turbulence intensity in feet per second, and Ω has units of radians per foot. The simulated wind conditions were for the turbulence length scale $L = 20$ ft, turbulence intensity $\sigma = 10$ ft/s, and over spatial frequencies Ω ranging from 10^{-4} to 1 rad/ft.

For the turning motion shown in Fig. 1, the simulation begins with a transition from constant altitude, wings level flight to helical descending flight. The helical path was chosen to demonstrate the robustness of the invariant EKF over the conventional EKF.

Process noise was superposed on the dynamics with covariance matrix $\boldsymbol{Q} = \mathrm{diag}(\mathbf{0}_3, \mathbf{0}_3, \sigma_{v_r}^2\mathbb{I}_3, \sigma_{\omega}^2\mathbb{I}_3, \sigma_{V_w}^2\mathbb{I}_3)$ where $\sigma_{v_r} = 0.01$, $\sigma_{\omega} = 0.001$, and $\sigma_{V_w} = 0.05$ (with commensurate units). Measurement noise with covariance matrix $\boldsymbol{R} = \sigma_v^2\mathbb{I}_{18}$ with $\sigma_v = 0.01$ was superposed on the output equation.

The invariant EKF was used to estimate the iner-

$$\boldsymbol{A}_k = \left.\frac{\partial \boldsymbol{f}_{\eta}}{\partial \boldsymbol{\eta}}\right|_{\boldsymbol{\eta}=\mathbf{0}} = \begin{pmatrix} \mathbf{0}_3 & \mathbf{0}_3 & \hat{\boldsymbol{R}}_{\mathrm{IB}}\boldsymbol{R}_{\gamma(\hat{\boldsymbol{x}})} & \mathbf{0}_3 & \mathbb{I}_3 \\ \mathbf{0}_3 & \mathbf{0}_3 & \mathbf{0}_3 & \hat{\boldsymbol{L}}_{\mathrm{IB}}\boldsymbol{R}_{\gamma(\hat{\boldsymbol{x}})} & \mathbf{0}_3 \\ \mathbf{0}_3 & \mathbf{0}_3 & -\boldsymbol{\omega}^{\times}(\boldsymbol{R}_{\gamma(\hat{\boldsymbol{x}})} + \mathbb{I}_3) & \boldsymbol{v}_{\mathrm{r}}^{\times}\boldsymbol{R}_{\gamma(\hat{\boldsymbol{x}})} & \mathbf{0}_3 \\ \mathbf{0}_3 & \mathbf{0}_3 & \mathbf{0}_3 & \begin{array}{c} -\boldsymbol{\omega}^{\times} - \boldsymbol{I}^{-1}\boldsymbol{\omega}^{\times}\boldsymbol{I}\boldsymbol{R}_{\gamma(\hat{\boldsymbol{x}})}^{\mathrm{T}} \\ +\boldsymbol{I}^{-1}(\boldsymbol{I}\boldsymbol{\omega})^{\times}\boldsymbol{R}_{\gamma(\hat{\boldsymbol{x}})}^{\mathrm{T}} \end{array} & \mathbf{0}_3 \\ \mathbf{0}_3 & \mathbf{0}_3 & \mathbf{0}_3 & \mathbf{0}_3 & \mathbf{0}_3 \end{pmatrix} \tag{11}$$

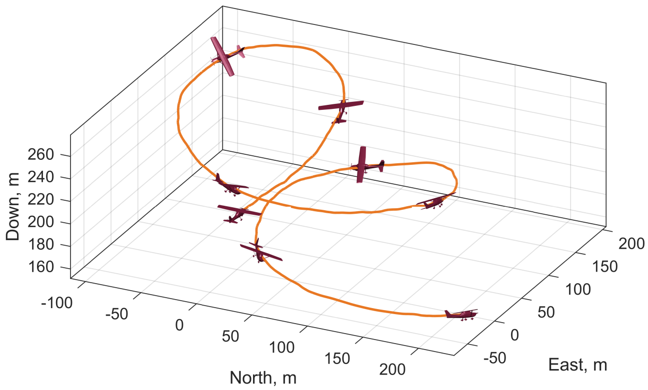

Figure 1: Trajectory of the fixed-wing UAV in a non-accelerated helical turn subject to a 1D von Kármán wind field.

tial position, orientation, body velocity, and body angular rate of the aircraft as well as the velocity of the wind. To initialize the filter, the initial state estimate $\hat{\boldsymbol{x}}(0) = (\boldsymbol{X}_0^{\mathrm{T}}, \boldsymbol{\Theta}_0^{\mathrm{T}}, \boldsymbol{v}_0^{\mathrm{T}}, \boldsymbol{\omega}_0^{\mathrm{T}}, \boldsymbol{V}_{w_0}^{\mathrm{T}})^{\mathrm{T}}$ was defined by choosing $\boldsymbol{X}_0 = (0, 0, -200)^{\mathrm{T}}$ m, $\boldsymbol{\Theta}_0 = (\frac{4\pi}{3}, \frac{5\pi}{4}, \frac{7\pi}{6})^{\mathrm{T}}$ rad, $\boldsymbol{v}_0 = (-20, 5, 50)^{\mathrm{T}}$ m/s, $\boldsymbol{\omega}_0 = (5, -5, 1)^{\mathrm{T}}$ rad/s, and $\boldsymbol{V}_{w_0} = (-25, -10, 15)^{\mathrm{T}}$ m/s. The filter was intentionally initialized using an initial condition far from the actual initial state of the simulated flight to illustrate convergence from nonzero initial error. The initial state error covariance matrix was set to $\boldsymbol{P}(0) = \mathbb{I}_{15}$. The IEKF estimates are compared to estimates obtained using a conventional EKF. Figure 2a shows the wind estimates obtained using the IEKF and the EKF for the two simulated trajectories. The EKF and invariant EKF were tuned using the same values for process and measurement noise covariance. A 10-second window of the wind estimation results is presented in Fig. 2b. These results show that both the EKF and the invariant EKF provide accurate estimates of wind velocity, however, the invariant EKF outperforms the conventional EKF.

Figure 3 shows root mean square (RMS) error of wind velocity estimates obtained using the invariant EKF and a conventional EKF in the two simulated flight conditions. The invariant EKF wind estimates have lower RMS error when compared to the EKF wind estimates.

6 Conclusions

This work presented the results of wind estimation for a small, fixed-wing UAV using the invariant EKF. The dynamics of the UAV were proven to be invariant under the action of the Lie group $G = SE(3)$ and the chosen output is G-equivariant. The design of the IEKF is described in five steps. The invariant EKF has stronger convergence guarantees over a larger subset of the state space as the

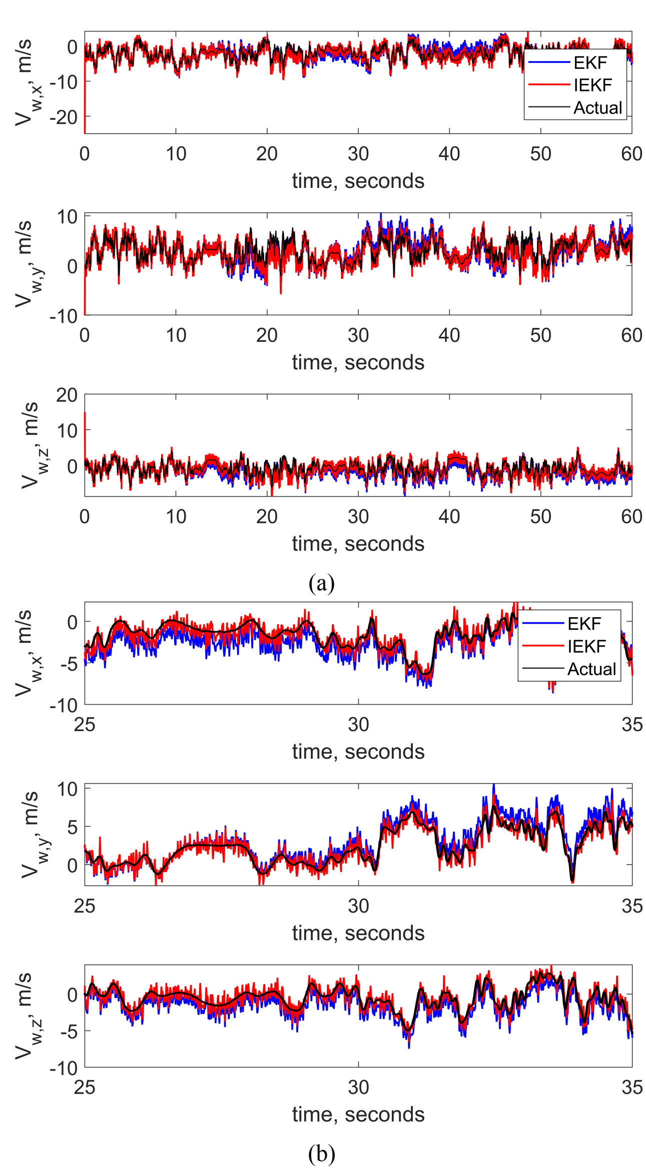

Figure 2: Wind estimation results using both the invariant EKF (denoted IEKF) and the conventional EKF (denoted EKF) compared to the actual simulated wind velocity values in flight corresponding a non-accelerated helical turn where in (a) the results are shown for the full simulation time and in (b) a 10-second window of the estimates is shown.

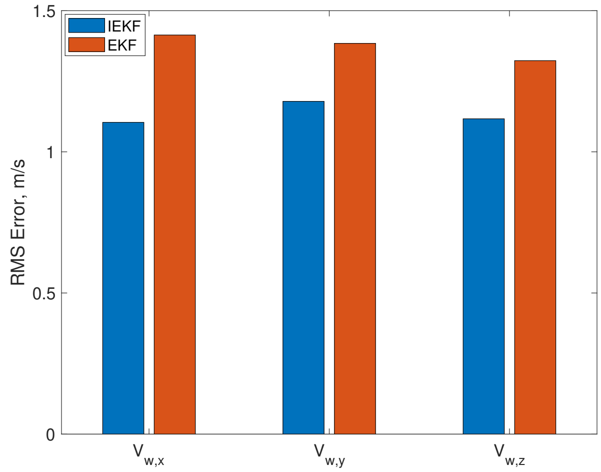

Figure 3: Root mean square error plots of wind estimates obtained using the invariant EKF and a conventional EKF for a non-accelerated helical turn.

Jacobian matrices defining the linearization remain relatively constant. Simulated flight data was generated for a non-accelerated helical turn where the nominal motion of the small, fixed-wing UAV was disturbed by 1D von Kŕmń turbulence. Wind estimates obtained using the invariant EKF were more accurate than those using the conventional EKF. Time histories of the true and estimated wind velocity clearly show better tracking by the invariant EKF supported quantitatively by the lower RMS error when compared to the EKF.

References

[1] Z. Ahmed and C. A. Woolsey. The Invariant Extended Kalman Filter for Wind Estimation using a Small Fixed-Wing UAV in Horizontal-Plane Flight.

[2] G. Balmer, T. Muskardin, S. Wlach, and K. Kondak. Enhancing model-free wind estimation for fixed-wing uav. In 2018 International Conference on Unmanned Aircraft Systems, pages 1242–1247. IEEE, 8 2018.

[3] L. Barbieri, S. T. Kral, S. C. Bailey, A. E. Frazier, J. D. Jacob, J. Reuder, D. Brus, P. B. Chilson, C. Crick, C. Detweiler, A. Doddi, J. Elston, H. Foroutan, J. González-Rocha, B. R. Greene, M. I. Guzman, A. L. Houston, A. Islam, O. Kemppinen, D. Lawrence, E. A. Pillar-Little, S. D. Ross, M. P. Sama, D. G. Schmale, T. J. Schuyler, A. Shankar, S. W. Smith, S. Waugh, C. Dixon, S. Borenstein, and G. D. Boer. Intercomparison of small unmanned aircraft system (suas) measurements for atmospheric science during the lapse-rate campaign. Sensors (Switzerland), 19, 5 2019.

[4] S. Bonnabel. Left-invariant extended kalman filter and attitude estimation. In 2007 46th IEEE Conference on Decision and Control, pages 1027–1032, 2007.

[5] S. Bonnabel, P. Martin, and P. Rouchon. Symmetry-preserving observers. IEEE Transactions on Automatic Control, 53(11):2514–2526, 2008.

[6] S. Bonnabel, P. Martin, and E. Salaün. Invariant extended kalman filter: theory and application to a velocity-aided attitude estimation problem. In Proceedings of the 48h IEEE Conference on Decision and Control (CDC) held jointly with 2009 28th Chinese Control Conference, pages 1297–1304, 2009.

[7] H. Chen, H. Bai, and C. N. Taylor. Invariant-ekf design for quadcopter wind estimation. In Proceedings of the 2022 American Control Conference (ACC), pages 1236–1241. IEEE, 6 2022.

[8] A. M. Cho, J. Kim, S. Lee, and C. Kee. Wind estimation and airspeed calibration using a uav with a single-antenna gps receiver and pitot tube. IEEE Transactions on Aerospace and Electronic Systems, 47, 2011.

[9] J.-P. Condomines, M. Bronz, G. Hattenberger, and J.-F. Erdelyi. Experimental wind field estimation and aircraft identification. In IMAV 2015: International Micro Air Vehicles Conference and Flight Competition, 2015.

[10] J. Cooper, J. Hopwood, C. Woolsey, S. D. Wekker, and M. DeVore. Intelligent wind estimation for chemical source localization. In VFS International 79th Annual Forum and Technology Display. Vertical Flight Society, 2023.

[11] S. F. J. De Wekker, M. Kossmann, J. C. Knievel, L. Giovannini, E. D. Gutmann, and D. Zardi. Meteorological applications benefiting from an improved understanding of atmospheric exchange processes over mountains. Atmosphere, 9(10), 2018.

[12] K. Gahan, J. W. Hopwood, and C. A. Woolsey. Wind estimation using an H∞ filter with fixed-wing aircraft flight test results. In AIAA SCITECH 2023 Forum, 2023.

[13] J. González-Rocha, S. F. D. Wekker, S. D. Ross, and C. A. Woolsey. Wind profiling in the lower atmosphere from wind-induced perturbations to multirotor uas. Sensors (Switzerland), 20, 3 2020.

[14] A. A. Jensen, J. O. Pinto, S. C. Bailey, R. A. Sobash, G. D. Boer, A. L. Houston, P. B. Chilson, T. Bell, G. Romine, S. W. Smith, D. A. Lawrence, C. Dixon, J. K. Lundquist, J. D. Jacob, J. Elston, S. Waugh, and M. Steiner. Assimilation of a coordinated fleet of uncrewed aircraft system observations in complex terrain: Enkf system design and preliminary assessment. Monthly Weather Review, 149:1459–1480, 5 2021.

[15] A. Kumar and P. Ben-Tzvi. Estimation of wind conditions utilizing rc helicopter dynamics. IEEE/ASME Transactions on Mechatronics, 24:2293–2303, 10 2019.

[16] J. W. Langelaan, N. Alley, and J. Neidhoefer. Wind field estimation for small unmanned aerial vehicles. Journal of Guidance, Control, and Dynamics, 34:1016–1030, 2011.

[17] P. P. Neumann and M. Bartholmai. Real-time wind estimation on a micro unmanned aerial vehicle using its inertial measurement unit. Sensors and Actuators, A: Physical, 235:300–310, 11 2015.

[18] P. J. Nolan, J. Pinto, J. González-Rocha, A. Jensen, C. N. Vezzi, S. C. Bailey, G. de Boer, C. Diehl, R. Laurence, C. W. Powers, H. Foroutan, S. D. Ross, and D. G. Schmale. Coordinated unmanned aircraft system (uas) and ground-based weather measurements to predict lagrangian coherent structures (lcss). Sensors (Switzerland), 18, 12 2018.

[19] R. T. Palomaki, N. T. Rose, M. van den Bossche, T. J. Sherman, and S. F. D. Wekker. Wind estimation in the lower atmosphere using multirotor aircraft. Journal of Atmospheric and Oceanic Technology, 34:1183–1191, 5 2017.

[20] J. Petrich and K. Subbarao. On-Board Wind Speed Estimation for UAVs. AIAA, 2011.

[21] D. Phelps, K. Gamagedara, J. Waldron, K. Patil, and M. Snyder. Ship air wake detection using a small fixed wing unmanned aerial vehicle. In AIAA Aerospace Sciences Meeting, 2018. AIAA, 2018.

[22] E. A. Pillar-Little, B. R. Greene, F. M. Lappin, T. M. Bell, A. R. Segales, G. B. H. D. Azevedo, W. Doyle, S. T. Kanneganti, D. D. Tripp, and P. B. Chilson. Observations of the thermodynamic and kinematic state of the atmospheric boundary layer over the san luis valley, co, using the coptersonde 2 remotely piloted aircraft system in support of the lapse-rate field campaign. Earth System Science Data, 13:269–280, 2 2021.

[23] M. B. Rhudy, Y. Gu, and H. Chao. Wind field velocity and acceleration estimation using a small uav. In Proceedings of the AIAA Modeling and Simulation Technologies Conference. AIAA, 6 2014.

[24] A. R. Segales, B. R. Greene, T. M. Bell, W. Doyle, J. J. Martin, E. A. Pillar-Little, and P. B. Chilson. The coptersonde: an insight into the development of a smart unmanned aircraft system for atmospheric boundary layer research. Atmospheric Measurement Techniques, 13:2833–2848, 5 2020.

[25] A. J. Torgesen, J. P. How, and B. Cameron. Airborne sensing for ship air wake surveys with a tethered autonomous uav. In AIAA Scitech 2021 Forum. AIAA, 2021.

[26] T. C. Wilson, J. Brenner, Z. Morrison, J. D. Jacob, and B. R. Elbing. Wind speed statistics from a small uas and its sensitivity to sensor location. Atmosphere, 13, 3 2022.

A Example Aircraft Parameters

The small, fixed-wing aircraft model used in simulation was the following MTD2 aircraft model identified by the Nonlinear Systems Laboratory (NSL) at Virginia Tech **?** . The mass and geometric properties of the MTD2 are provided in Table 1.

Table 1: MTD2 aircraft mass and geometric properties.

Parameter	Symbol	Value
Mass	m	3.311 kg
Moments of inertia	I_{xx}	0.319 kg-m^2
	I_{yy}	0.267 kg-m^2
	I_{zz}	0.471 kg-m^2
	I_{xz}	0.024 kg-m^2
Wing span	b	1.80 m
Mean aerodynamic chord	c	0.254 m
Wing surface area	S	0.457 m^2
Propeller diameter	D	0.254 m
Number of propellers	η_n	2
Propeller Efficiency	η_e	90%

An identified aerodynamic model of the aircraft was used to simulate its flight. The model was identified from flight data by other members of the NSL. The models identified for the aerodynamic force and moment are

$$\boldsymbol{F}_{\text{A}} = \frac{1}{2}\rho\|\boldsymbol{v}\|^2 S \begin{pmatrix} C_X(\boldsymbol{v},\boldsymbol{\omega},\boldsymbol{\delta}) \\ C_Y(\boldsymbol{v},\boldsymbol{\omega},\boldsymbol{\delta}) \\ C_Z(\boldsymbol{v},\boldsymbol{\omega},\boldsymbol{\delta}) \end{pmatrix} + \xi \begin{pmatrix} C_J(\boldsymbol{\delta}) \\ 0 \\ 0 \end{pmatrix} \tag{14}$$

$$\boldsymbol{M}_{\text{A}} = \frac{1}{2}\rho\|\boldsymbol{v}\|^2 S \begin{pmatrix} bC_l(\boldsymbol{v},\boldsymbol{\omega},\boldsymbol{\delta}) \\ \bar{c}C_m(\boldsymbol{v},\boldsymbol{\omega},\boldsymbol{\delta}) \\ bC_n(\boldsymbol{v},\boldsymbol{\omega},\boldsymbol{\delta}) \end{pmatrix} \tag{15}$$

where $\xi = D^4\rho\eta_e\eta_{\text{n}}\delta_{\text{rps}}^2$ and $\boldsymbol{\delta} = [\delta_a, \delta_e, \delta_r, \delta_{\text{rps}}]^{\text{T}}$ are the control inputs corresponding to aileron, elevator, rudder, and thrust commands, $\bar{c}$ is the mean aerodynamic chord, b is the wingspan, S is the aircraft wing surface area, ρ is the air density, D is the diameter of the propeller, η_e is the propeller efficiency, and η_n is the number of propellers. The non-dimensional thrust, force, and moment models are

$$C_J = C_{J_0} + C_J J + C_{J^2} J^2 \tag{16a}$$

$$C_X = C_{X_0} + C_{X_{\delta_e}}\delta_e + C_{X_\alpha}\alpha + C_{X_\alpha^2}\alpha^2 \tag{16b}$$

$$C_Y = C_{Y_p}\hat{p} + C_{Y_{\text{r}}}\hat{r} + C_{Y_{\delta_a}}\delta_a + C_{Y_{\delta_{\text{r}}}}\delta_{\text{r}} + C_{Y_\beta}\beta \tag{16c}$$

$$C_Z = C_{Z_0} + C_{Z_q}\hat{q} + C_{Z_\alpha}\alpha \tag{16d}$$

$$C_l = C_{l_p}\hat{p} + C_{l_{\delta_a}}\delta_a + C_{l_\beta}\beta \tag{16e}$$

$$C_m = C_{m_0} + C_{m_q}\hat{q} + C_{m_{\delta_e}}\delta_e + C_{m_\alpha}\alpha + C_{m_{\dot{\alpha}}}\dot{\alpha} \tag{16f}$$

$$C_n = C_{n_{\text{r}}}\hat{r} + C_{n_{\delta_a}}\delta_a + C_{n_{\delta_{\text{r}}}}\delta_{\text{r}} + C_{n_\beta}\beta \tag{16g}$$

where the non-dimensional terms in Eqn. (16) are

$$\alpha = \tan^{-1}\left(\frac{w}{u}\right) \quad \beta = \sin^{-1}\left(\frac{v}{\|\boldsymbol{v}\|}\right) \quad \hat{p} = \frac{pb}{2\|\boldsymbol{v}\|}$$

$$\hat{q} = \frac{q\bar{c}}{2\|\boldsymbol{v}\|} \qquad \hat{r} = \frac{rb}{2\|\boldsymbol{v}\|} \qquad J = \frac{\|\boldsymbol{v}\|}{\delta_{\text{rps}}D}$$

Table 2 provides the identified force and moment coefficients.

Table 2: Aerodynamic force and moment coefficients for the MTD2.

Coefficient	Value	Coefficient	Value
C_{J_0}	-0.131	C_{Y_p}	0.221
C_J	-0.040	C_{Y_r}	0.230
C_{J^2}	0.116	$C_{Y_{\delta_a}}$	0.118
C_{X_0}	-0.428	$C_{Y_{\delta_r}}$	0.136
$C_{X_{\delta_e}}$	0.051	C_{Y_β}	-0.525
C_{X_α}	0.282		
$C_{X_{\alpha^2}}$	3.292		
Coefficient	**Value**	**Coefficient**	**Value**
C_{Z_0}	-0.225	C_{m_0}	0.008
C_{Z_q}	-12.54	C_{m_q}	-14.02
C_{Z_α}	-4.451	$C_{m_{\delta_e}}$	-0.415
		C_{m_α}	-0.471
		$C_{m_{\dot{\alpha}}}$	0.550
Coefficient	**Value**	**Coefficient**	**Value**
C_{l_p}	-0.386	C_{n_r}	-0.119
$C_{l_{\delta_a}}$	-0.137	$C_{n_{\delta_a}}$	0.013
C_{l_β}	-0.039	$C_{n_{\delta_r}}$	-0.068
		C_{n_β}	0.103